Electronic Supplementary Information (ESI)

Janus Architecture Host Electrode for Mitigating Lithium-Ion Polarization in High-Energy-Density Li-S Full Cells

Kyungsik Um[†], *Chanho Jung*[†], *Hyunsuk Nam, Haeli Lee, Saegi Yeom, Jun Hyuk Moon*[*]

Department of Chemical and Biological Engineering, Korea University, 145 Anam-ro, Seongbuk-gu, Seoul, 02841, Republic of Korea

[†]*These authors contributed equally to this work.*

[*]*Corresponding author, E-mail: junhyukmoon@korea.ac.kr*

Experimental Section

Synthesis of Mo_2C-coated CNT/CF film: Mo_2C-coated CNT/CF films were synthesized through a modified thermal annealing method, utilizing ammonium molybdate (Sigma-Aldrich, 99.98%) as the molybdenum (Mo) precursor. The synthesis began by dissolving ammonium molybdate in distilled water at specified ratios, followed by stirring the solution for 30 minutes. This solution was then drop-casted onto CNT/CF films, with the volume of the solution adjusted according to each substrate film. After drop-casting, the films were dried at 90°C for 3 hours. These ammonium molybdate-CNT/CF composites were then annealed in a tube furnace at 800°C for 6 hours under an argon (Ar) atmosphere. For the cathode, the Janus film was produced by calendering a bare CNT film alongside a 20 wt% Mo_2C-coated CNT film, creating a film with two distinct surfaces: one with a Mo_2C coating and the other uncoated. Similarly, for the anode, a 20 wt% Mo_2C-coated CF film was calendered with a bare CF film. As a control, uniform films were constructed for both cathode and anode by stacking two Mo_2C-coated CNT/CF films, with mass ratios of 20 wt%, respectively.

Material Characterization: The surface and cross-sectional microstructures were characterized using field-emission scanning electron microscopy (FE-SEM, JSM-7100F) and transmission electron microscopy (TEM, JEM-3010, JEOL). X-ray diffraction (XRD) analysis was performed using a Davinci D8 Advance diffractometer, with a scan rate of 0.05° s^{-1} across scan ranges from 10° to 80°. X-ray photoelectron spectroscopy (XPS) data were collected using a Leybold spectrometer equipped with an Al Kα monochromatic beam (1486.6 eV, 150 W input power, ESCALAB250 XPS system, Theta Probe XPS system). The specific surface areas were determined by the Barrett-Emmett-Teller (BET) method (ASAP 2020, Micromeritics Inc.). Raman spectra were acquired in the range of 200–1600 cm^{-1} using an excitation wavelength of 532 nm (Horiba-iHR550). Thermogravimetric analysis (TGA) was conducted from 25 to 900 °C in air at a heating rate of 10 °C min^{-1} (TG, TA Instruments, Q5000 IR). To assess the adsorption on the cathode host substrate, a Li_2S_6-containing electrolyte solution was prepared; this was achieved by mixing Li sulfide (Li_2S, Merck) and S powder (S_8, Alfa Aesar) at a molar ratio of 8:5 in a 1:1 volume ratio of DOL/DME at 90 °C. After allowing the host substrate to undergo adsorption for 3 hours, the quantity of adsorption was determined by recording the UV-Vis spectra. For *ex-situ* XPS analysis on the anode, the cells were carefully disassembled within an Ar-filled glove box, and the anodes were vacuum-sealed to prevent any unnecessary oxidation and side reactions of the Li metal anode. The XPS analysis was conducted on anode

samples at various cycles. The collected data were normalized based on the peak intensities of Li_2SO_3 and Li_2SO_4, indicative of the formation of the solid-electrolyte interface (SEI) layer.

Electrochemical analysis: All electrochemical tests were conducted using a Maccor 4300 Battery Test System. Galvanostatic charge and discharge tests were performed within a voltage range of 1.7 – 2.8 V (vs. Li/Li^+). Cyclic voltammetry tests were carried out over the same voltage range at scan rates varying from 0.2 mV s^{-1} to 0.5 mV s^{-1}, at a test temperature of 30 °C. Electrochemical performance data were obtained from an average of three experimental runs (error bars and standard deviation were not shown for convenience), and the specific capacity was calculated based on the mass of sulfur in the cathode, employing a theoretical capacity of 1675 mAh g^{-1}. This calculation was predicated on the average coulombic efficiency (CE) value of samples being greater than 99%. The electrochemical impedance spectrum (EIS) was recorded using an impedance analyzer (Versastat, AMETEK), scanning frequencies from 0.1 Hz to 1 MHz with a voltage amplitude set at 10 mV. Shuttle current measurements utilized an electrolyte devoid of $LiNO_3$ to avoid Li anode passivation. In this setup, cells were initially charged to 2.8 V (0.1 C current density) and subjected to 10 charging/discharging cycles. Following the last charge, cells were discharged to 2.38 V and transitioned to potentiostatic mode to peak the shuttle current. This current stabilized after about 300 seconds, defining the observed shuttle current. For potentiostatic discharge to form Li_2S, cells were assembled with Li_2S_6 catholyte. Specifically, the cells were first discharged galvanostatically to 2.05 V, followed by potentiostatic discharge at 2.05 V. The final capacities for Li_2S precipitation were calculated based on Faraday's law. For the galvanostatic Li deposition test, Li metal served as the counter electrode. Measurements were conducted at a current density of 1 mA cm^{-2} to achieve a capacity of 10 mAh cm^{-2}. Coulombic efficiency was determined at a current density of 1 mA cm^{-2} within a potential range of -1.0 V to 1.0 V (vs. Li/Li^+), using a Li-plated Cu substrate as the counter electrode. The long-term cyclic stability of the anode host was assessed at various current densities ranging from 2 to 10 mA cm^{-2}. Li symmetric cells, used for testing cycling ability, were assembled with identical working and counter electrodes.

Assembly of Li-S cells: Li-S cells were assembled in an argon-filled glove box under a controlled humidity environment (<0.01 ppm H_2O, <0.01 ppm O_2). Sulfur loading on the cathode substrate was achieved through conventional melt diffusion, with a typical loading content of approximately 62.5 wt% relative to the cathode substrate. The electrolyte solution, consisting of 1 M bis(trifluoromethane) sulfonimide Li salt (LiTFSI, Sigma-Aldrich) and 0.2 M Li nitrate ($LiNO_3$, Alfa Aesar) dissolved in a 1:1 v/v% mixture of 1,3-dioxolane (DOL,

Sigma-Aldrich) and dimethoxyethane (DME, Sigma–Aldrich), was used. The Li anode substrates were pre-deposited with Li at varying areal capacities ranging from 16.75 to 33.5 mAh cm^{-2}. Specifically, S/Janus||Li cells are consisted of a Janus cathode paired with Li metal foil, while S/CNT||Janus/Li cells featured an S-loaded CNT film cathode and a Li pre-deposited Janus anode. Full cells were utilized with both Janus cathode and anode configurations. The thickness of the cathode electrode was controlled within the range of 100-200 μm, and the thickness of the anode was similarly controlled within 100-200 μm.

DFT calculation: DFT calculations were performed using the Quantum ESPRESSO package. The interaction between core and valence electrons was modeled using the frozen-core projector augmented wave (PAW) method. The exchange-correlation functional employed was the generalized gradient approximation (GGA) in the form of Perdew-Burke-Ernzerhof (PBE), with van der Waals (vdW) interactions incorporated via Grimme's DFT-D3 method. Electronic wavefunctions were expanded using a plane-wave basis set with a cutoff energy of 5000 eV. The Brillouin zone was sampled with 3x3x3 k-point Monkhorst-Pack meshes, and a vacuum layer of 15 Å was introduced in the (101) direction to avoid interactions between periodic images. The calculations were carried out to an energy precision of 10^{-5} eV, allowing atomic coordinates to relax until the maximum residual force was below 0.01 eV $Å^{-1}$. The binding energy (E_B) between Li_2S_6 and metal oxide is calculated using the formula,

$$E_B = E(Li_2S_6+sub) - E(Li_2S_6) - E(sub)$$

where $E(Li_2S_6+sub)$, $E(Li_2S_6)$, and $E(sub)$ denote the energy for the Li_2S_6-adsorbed system, Li_2S_6, and substrate, respectively.

Supplementary Note #1

We calculate the specific energy for various sulfur loadings, N/P ratios, and E/S ratios using the formula below.

$$Cell\ Energy = \frac{1675\ mAh\ g^{-1} \times S_{sulfur\ utilization}\% \times m\ mg\ cm^{-2}}{\frac{m\ mg\ cm^{-2}}{W_{sulfur}\%} + \frac{n \times 1675\ mAh\ g^{-1} \times m\ mg\ cm^{-2}}{3860\ mAh\ g^{-1}} + m\ mg\ cm^{-2} \times E}$$

where sulfur loading is denoted as m, the volume of electrolyte is E, and the N/P ratio is n.

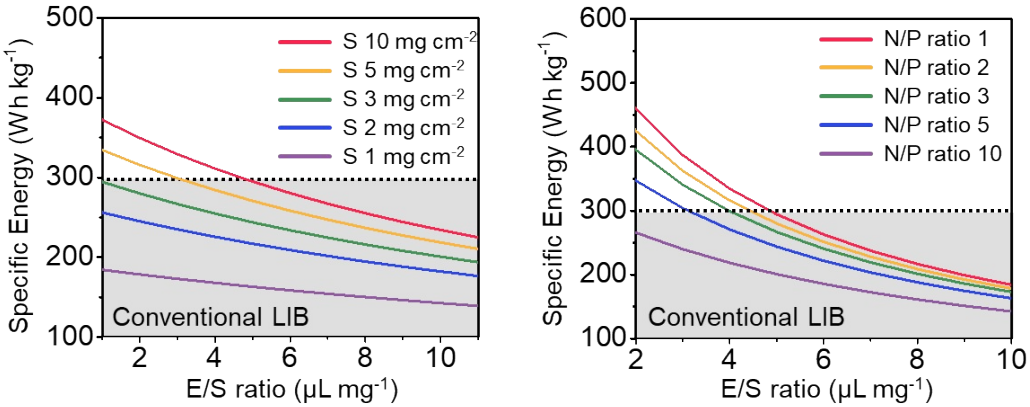

The graph presents a plot of E/S versus specific energy, with the left side showing variations in sulfur loading and the right side displaying variations in the N/P ratio. To surpass the energy density of conventional LIBs, which is approximately 300 Wh kg^{-1},[1, 2] the E/S ratio must be less than 3 μL mg^{-1}, the sulfur loading must be greater than 5 mg cm^{-2}, and the N/P ratio should be no more than 5.

Supplementary Note #2

The concentration of lithium ions within a porous electrode can be described by the Nernst-Planck equation:

$$J_i = -D_i\frac{dC_i}{dx} - u_i c_i z_i F\frac{dV}{dx}$$

where J is the ion flux, D is the diffusion coefficient, C is the ion concentration, u is the ion mobility, and V is the voltage. [2]

In the high current density environments typical of batteries, the ion flux is controlled by ion diffusion. Then, the distribution of lithium ion concentrations across the electrode thickness, denoted by x, is presented as follows:

$$C_{Li^+} = C^{0}_{Li^+} - \frac{3C^{0}_{Li^+}}{\pi}\sum_{n=0}^{\infty}\frac{(-1)^n}{2n+1}\exp\left\{-\frac{(2n+1)^2\pi^2 Dt}{4\quad l^2}\right\}\cos\left\{\frac{(2n+1)\pi x}{2l}\right\}$$

where C_{Li^+} represents the concentration of lithium ions, $C^{0}_{Li^+}$ is the concentration of lithium ions at the top surface of the electrode, and l is the electrode thickness. Based on a 50-μm-thick electrode, the concentration profile of lithium ions at various electrode thicknesses is shown in the figure below. Note that at an electrode thickness of 150 micrometers, the concentration difference between the top surface and the bottom is as much as 50%.[3, 4]

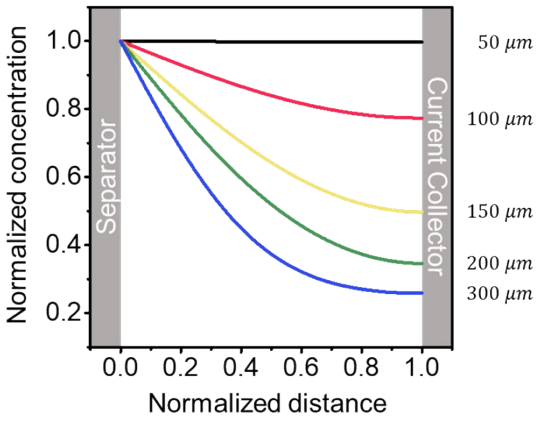

Supplementary Note #3

To determine the diffusion coefficient of lithium ions diffusing into the electrode, we apply the Randles-Sevcik equation:

$$I_p = 2.69 \times 10^5 n^{1.5} A D^{0.5} C v^{0.5}$$

where I_p (A) is the peak current peak, n is the number of electrons per reaction species, A (cm^2) is the area of the electrode, D ($cm^2\ s^{-1}$) is the diffusion coefficient, C (mol mL^{-1}) is the concentration of Li-ion concentration, v (V s^{-1}) is the scan rate.

The lower left graph presents the cyclic voltammetry results for the Janus film and the uniform Mo_2C film substrate cathodes at various scan rates. The slope of the plot of the square root of the scan rate versus the absolute value of the peak current is related to the diffusion coefficient. We applied the Randles-Sevcik equation to the second cathodic peak to compare the diffusion coefficients (D) and found that D is twice as high for the Janus film compared to the uniform film. This finding suggests a more uniform polysulfide conversion across the electrode in the Janus film.

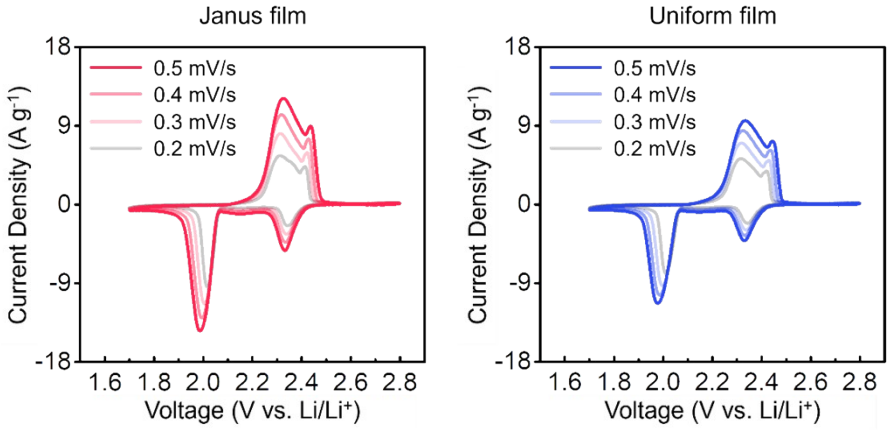

Fig.. Cyclic voltammetry analysis of Janus film and uniform Mo_2C-coated CNT film cathode.

We infer the extent of Li-ion polarization improvement from the enhanced diffusion observed in the Janus film. The lower right graph shows that the polarization is improved by 60% in the Janus film compared to the uniform film.

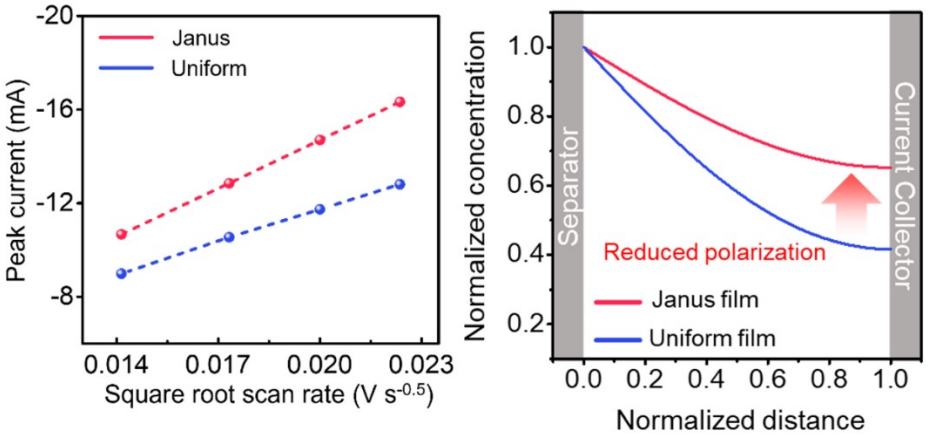

Fig.. (left) Cathodic current plotted against the square root of the scan rate. (right) Li-ion polarization on the Janus and uniform film substrates, respectively.

Supplementary Note #4

At 0.1 mAh cm^{-2}, the formation of the SEI layer is visible, with no significant differences between the two anode hosts. SEM and EDS mapping images reveal an SEI layer composed of S, F, and O elements.[5, 6] At 1 mAh cm^{-2}, unlike the Janus film, the uniform film exhibits Li plating beginning from the top surface where the diffusion path of Li-ions is shorter. At 2 mAh cm^{-2}, continuous top growth is observed in the uniform film, whereas the Janus film shows a surface that remains fibrous, similar to the condition at 1 mAh cm^{-2}. This supports that in the Janus film, Li nucleation begins underneath the electrode coated with Mo_2C. At 5 mAh cm^{-2}, the uniform film displays a dendritic surface in the Li plating, while the Janus film still shows no top growth.

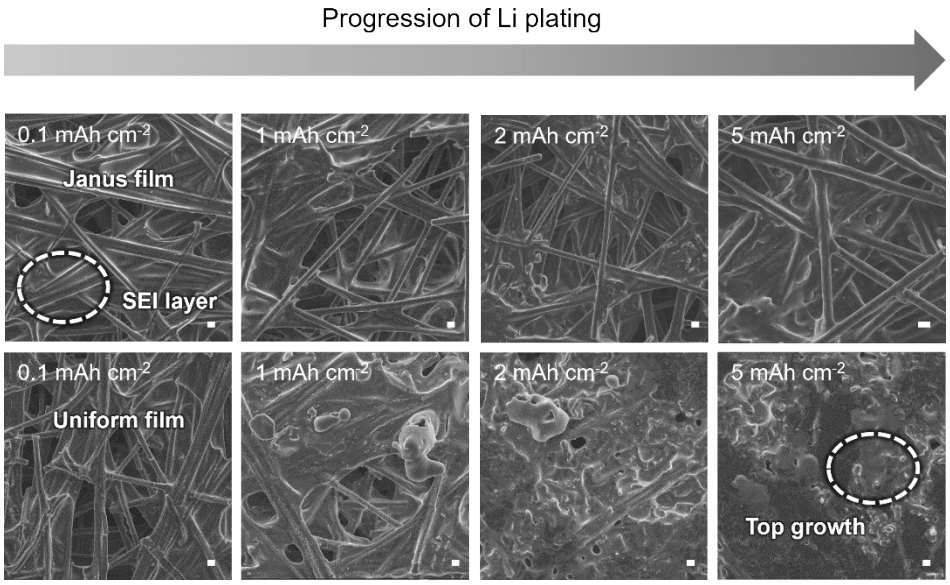

Fig.. *ex-situ* SEM images of Janus and uniform film anode hosts during Li plating. (Scale bar: 1 μm)

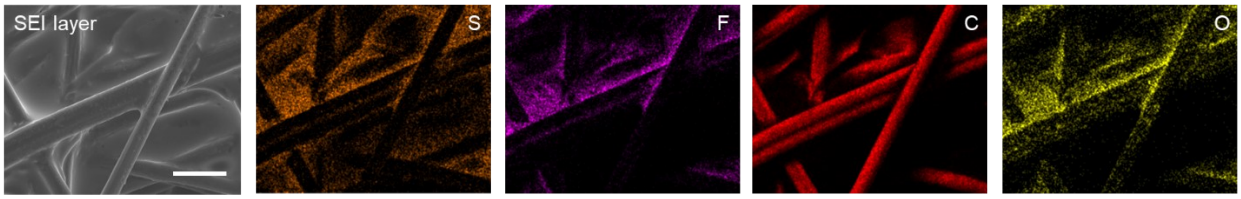

Fig.. Initial Li plating on the surface of Janus film host with SEM and EDS mapping.

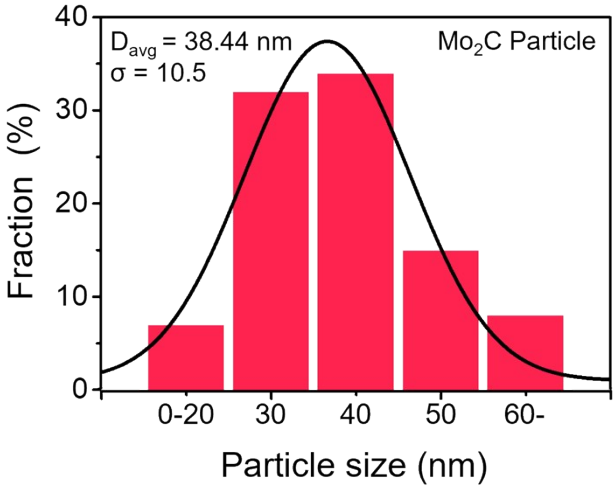

Fig. S1. Mo_2C particle size distribution.

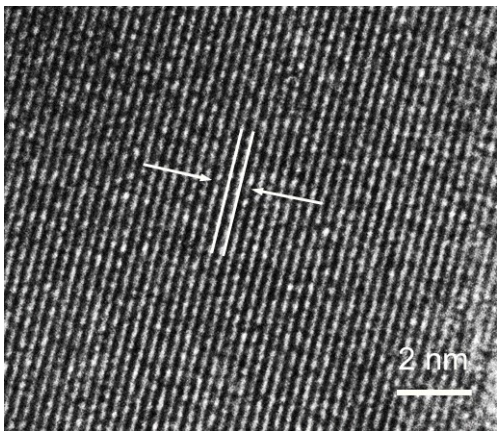

Fig. S2. HRTEM image of Mo_2C nanoparticles. The lattice fringe corresponding to the (101) plane of Mo_2C measures 0.228 nm. (Scale bar: 2 nm)

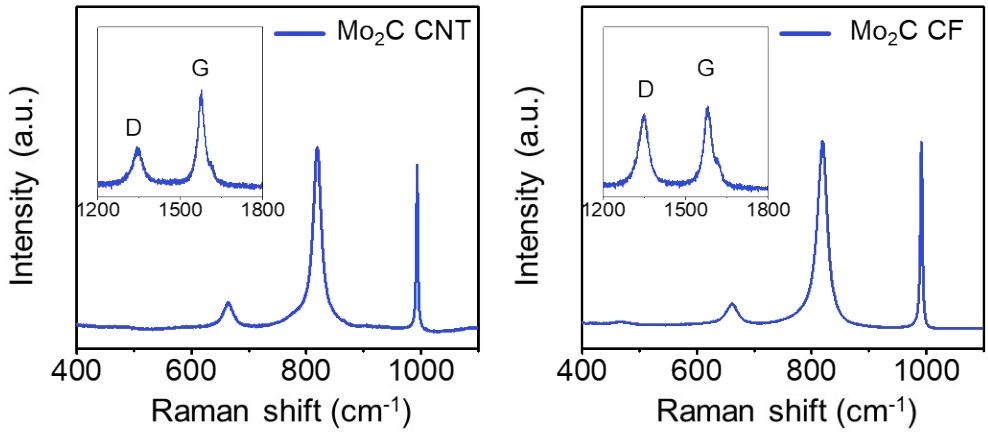

Fig. S3. Raman spectrum of Mo_2C-coated CNT film (left) and Mo_2C-coated CF film (right). Peaks at 666 cm^{-1}, 823 cm^{-1}, and 995 cm^{-1} are attributed to the hexagonal phase of Mo_2C, while peaks at 1358 cm^{-1} and 1570 cm^{-1} correspond to the D and G peaks of carbon.[7]

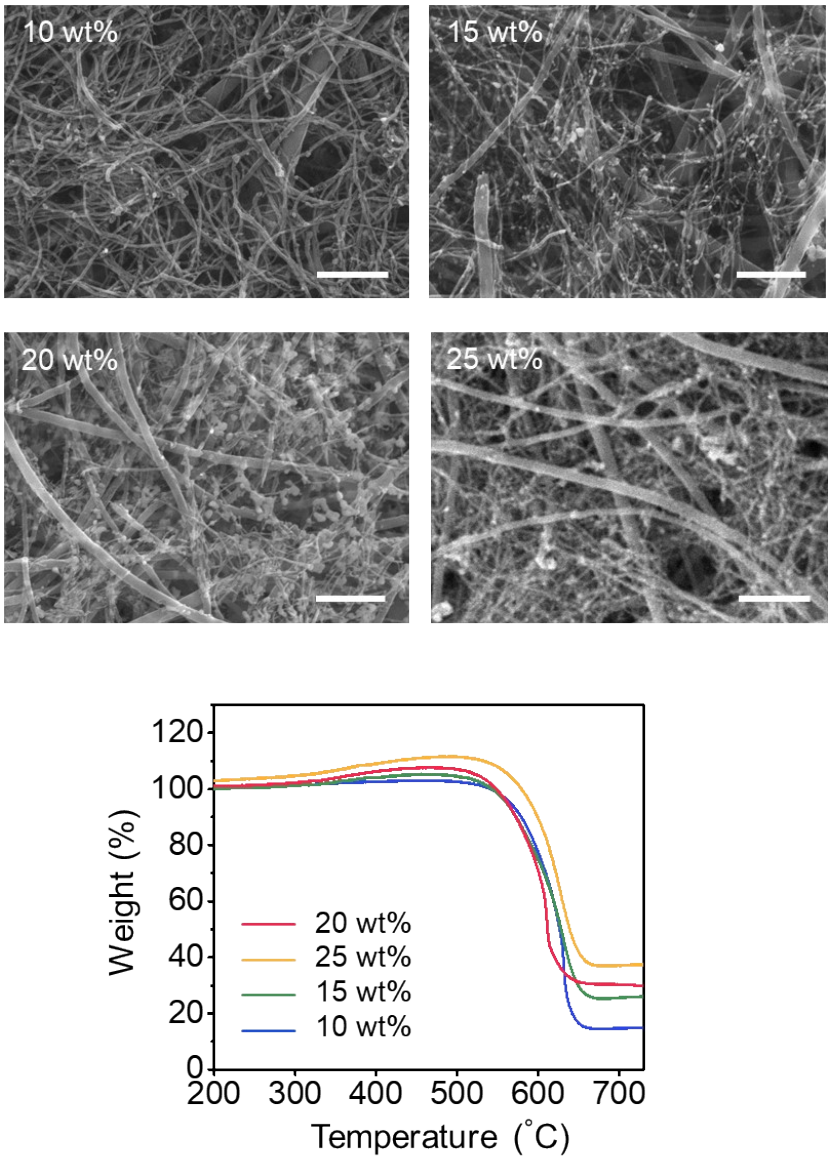

Fig. S4. SEM images of Mo_2C-CNT with varying Mo_2C coating weights (top panel). The degree of coating was controlled by adjusting the concentration of the precursor solution, and the content was estimated through TGA analysis [8, 9] (bottom panel). (Scale bar: 1μm)

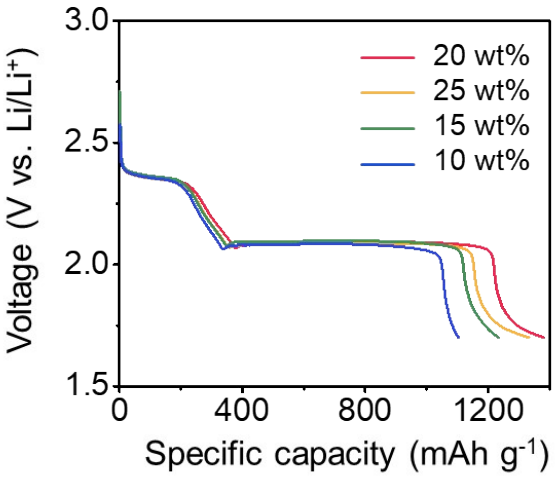

Fig. S5. Discharge profiles of cells with Mo_2C-CNT cathode hosts at various Mo_2C coating contents. The cathode capacity was evaluated under conditions of 1 mg cm^{-2} S loading at 0.5 C. The highest capacity observed was 1380 mAh g^{-1} at 20 wt%, leading us to choose a Mo_2C coating content of 20 wt%.

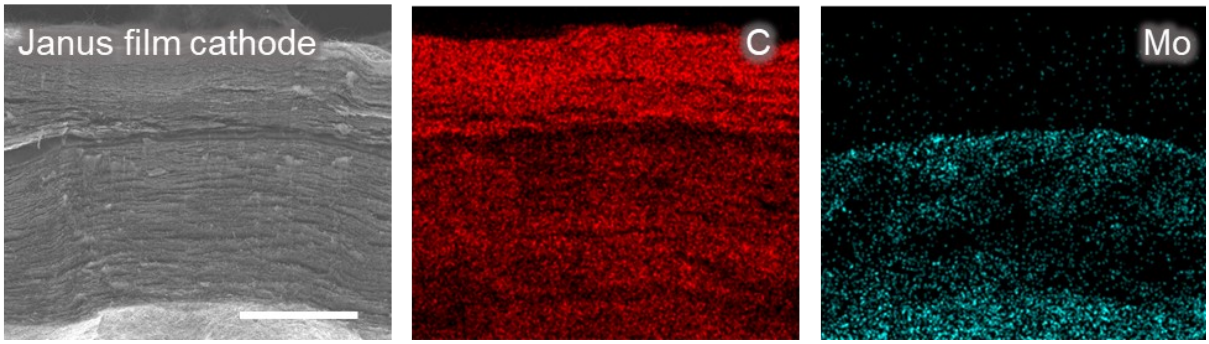

Fig. S6. Cross-sectional SEM and corresponding EDS mapping images of the Janus film cathode host substrate. Mo_2C coating is observed only in the lower half of the film. (Scale bar: 100 μm)

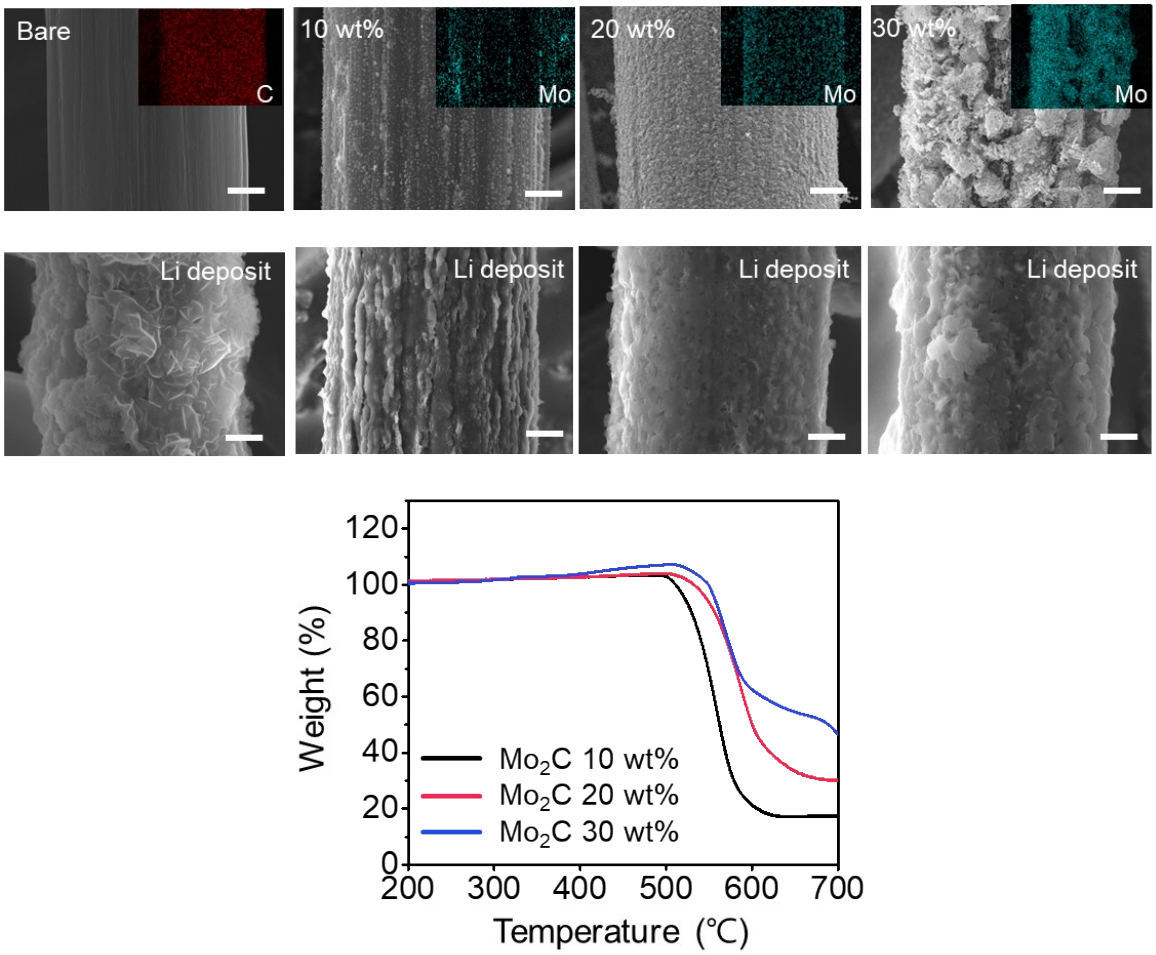

Fig. S7. (Top Panel) SEM/EDS images of bare carbon fiber and carbon fibers coated with 10 - 30 wt% Mo_2C. SEM images of Li deposition on each Mo_2C-CF used as an anode substrate. The most uniform Li deposition is observed on the 20 wt% Mo_2C-CF. (Scale bar: 1 μm) (Bottom Panel) TGA analysis of carbon fibers coated with varying amounts of Mo_2C; the result shows coatings of approximately 10 wt%, 20 wt%, and 30 wt%.

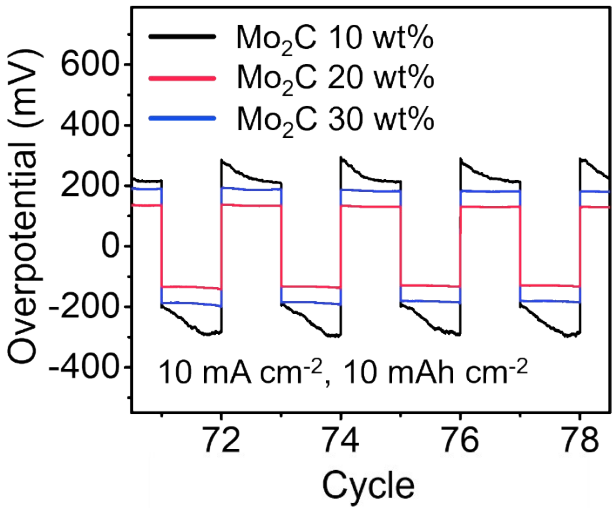

Fig. S8. Galvanostatic plating/stripping cycle profiles for Mo_2C-CF anode substrates with various Mo_2C coating contents. These measurements were conducted using a symmetric cell at a current density of 10 mA cm^{-2} for a capacity of 10 mAh cm^{-2}. A 20 wt% coating shows the lowest voltage hysteresis, which justifies the use of this coating.

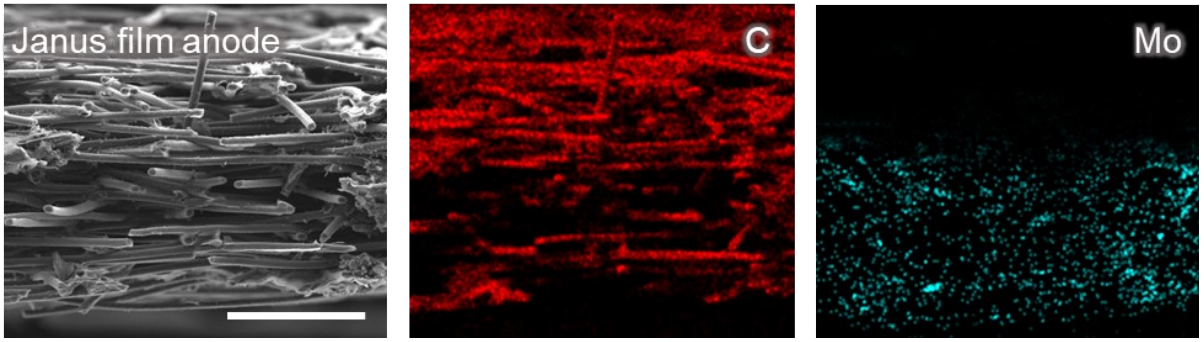

Fig. S9. Cross-sectional SEM and corresponding EDS mapping images of the Janus film anode substrate. It is observed that Mo_2C is coated only on the lower half of the film. (Scale bar: 100 μm)

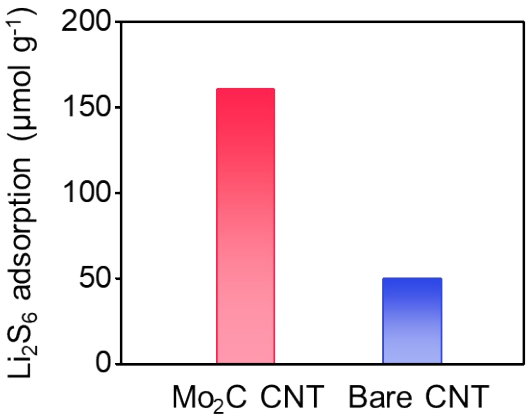

Fig. S10. Li_2S_6 adsorption amounts on Mo_2C-CNT and bare CNT films. Mo_2C-CNT exhibits approximately 3.2 times higher adsorption compared to bare CNT, which is attributed to the higher adsorptive capacity of Mo_2C.

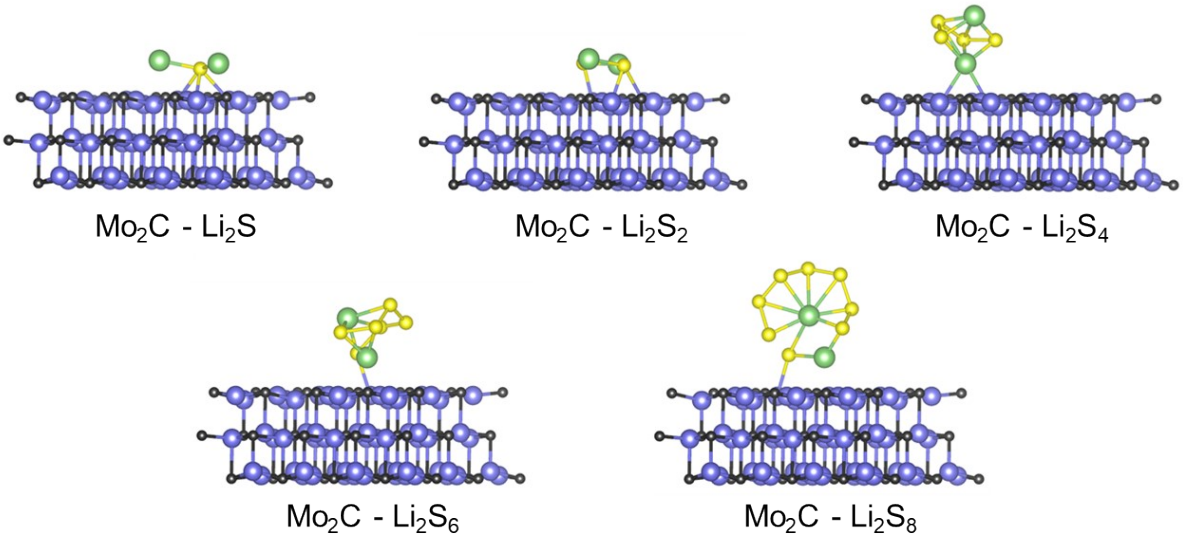

Fig. S11. Individual atomic configuration images of optimized adsorption of Li_2S_n (n = 1, 2, 4, 6, 8) on the Mo_2C (101) surface.

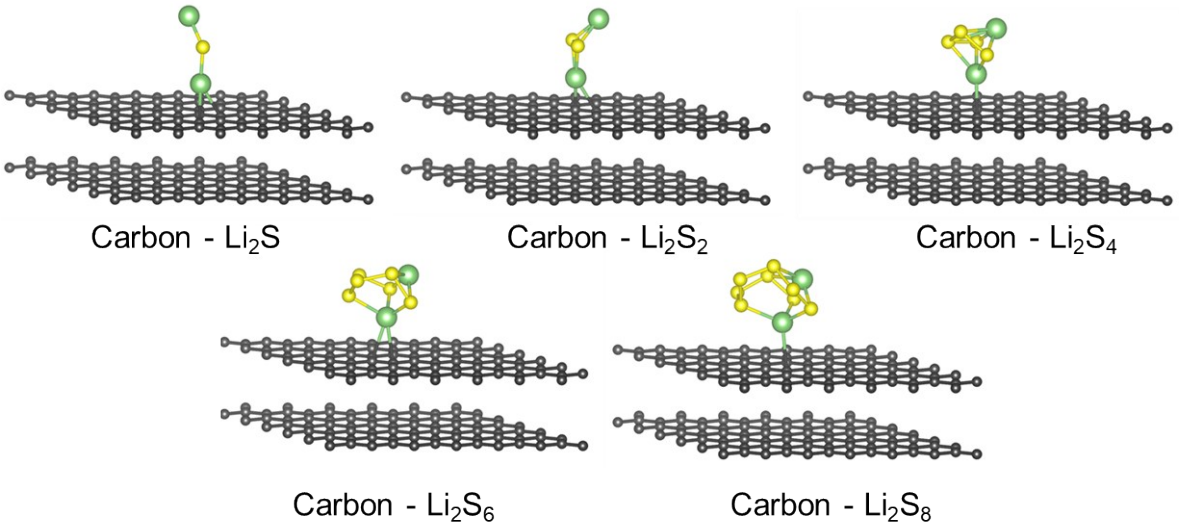

Fig. S12. Individual atomic configuration images of optimized adsorption of Li_2S_n (n = 1, 2, 4, 6, 8) on a carbon (graphene) surface.

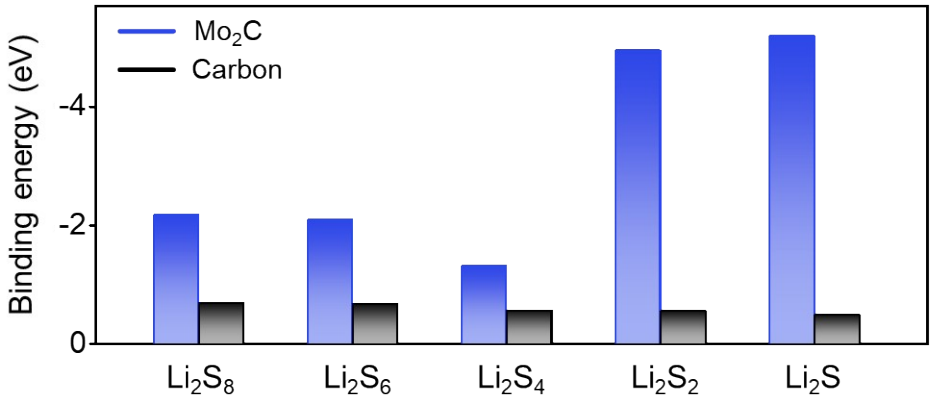

Fig. S13. DFT calculations of binding energies for the adsorption of Li_2S_n (n = 1, 2, 4, 6, 8) on surfaces of Mo_2C (101) and carbon substrates.

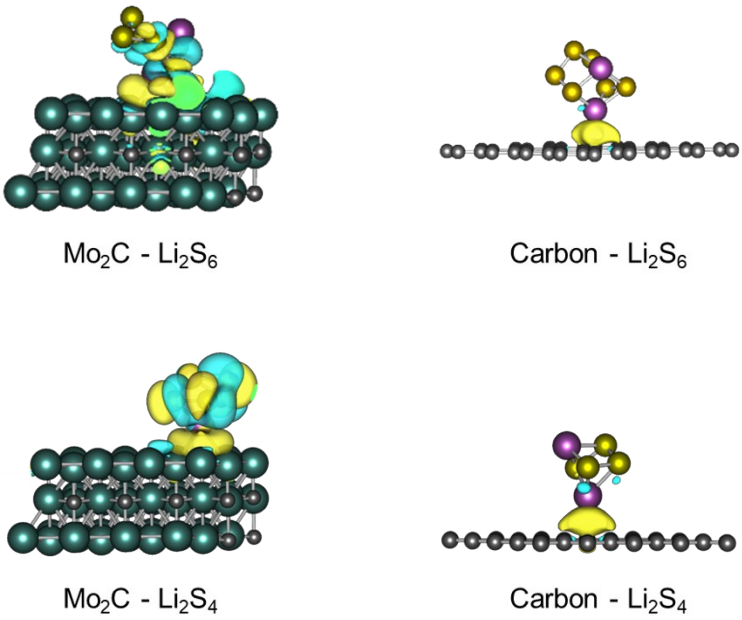

Fig. S14. Differential charge density images for Li_2S_6 and Li_2S_4 adsorbed on Mo_2C and carbon surfaces, respectively. The higher differential charge density on Mo_2C indicates that the adsorption of lithium polysulfides on this substrate has a covalent bonding nature.[10, 11]

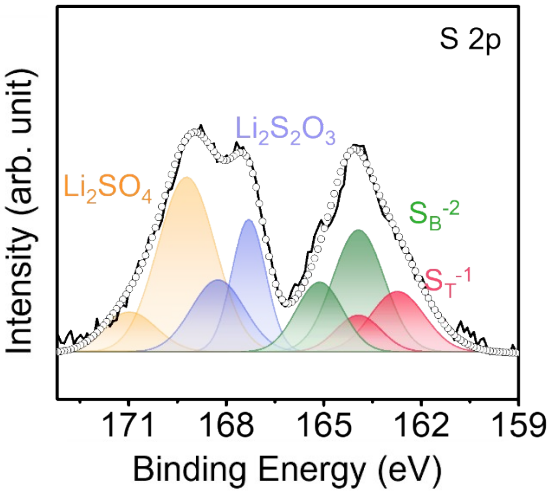

Fig. S15. S 2p XPS spectrum of Mo_2C after the adsorption of Li_2S_6.[12, 13]

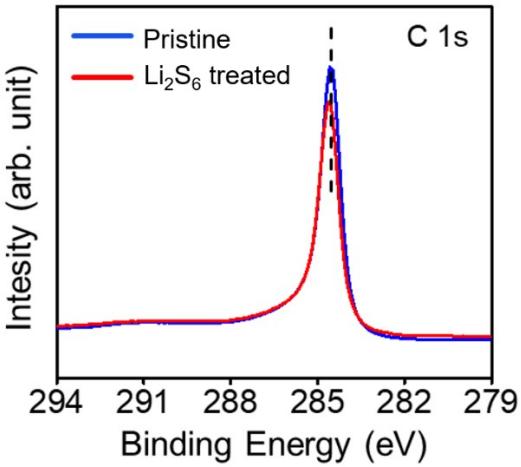

Fig. S16. C 1s XPS spectrum of Mo_2C before and after the adsorption of Li_2S_6. No shift is observed after Li_2S_6 adsorption, indicating that carbon does not form a strong bond with sulfur.[14]

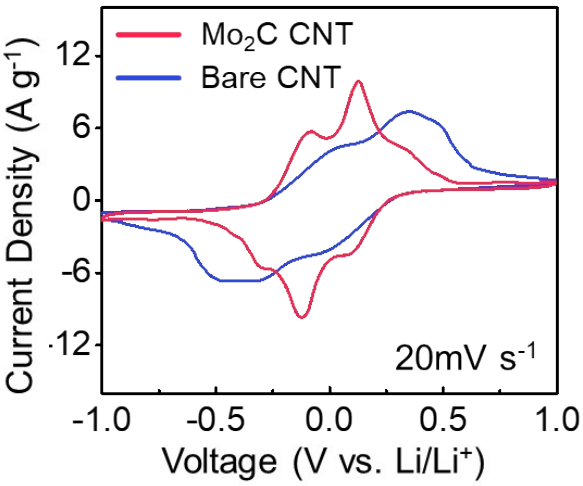

Fig. S17. Cyclic voltammetry curves of symmetric cells for Mo_2C CNT and bare CNT film cathode hosts. Measurements were conducted at a scan rate of 20 mV s^{-1} within a voltage range of -1.0 to 1.0 V. The curves display cathodic and anodic peaks corresponding to the conversion of Li_2S_6 into lower-order LiPS molecules and the reverse process, respectively. Compared to the bare CNT substrate, the Mo_2C-CNT substrate exhibits higher peak current densities and reduced polarization between the redox peaks, indicating superior conversion kinetics on Mo_2C.

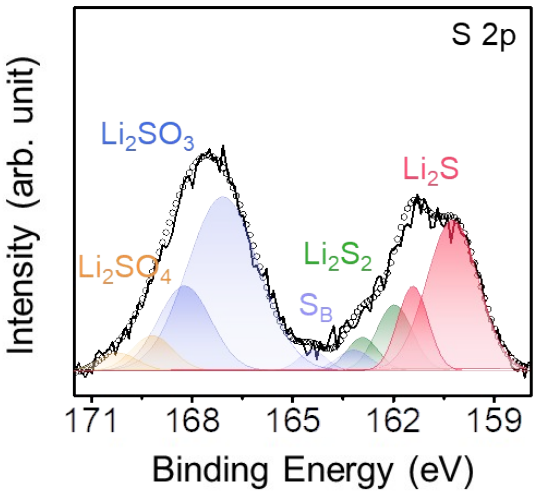

Fig. S18. *ex-situ* S 2p XPS of the Li anode from a bare CNT cell after 10 cycles. Unlike the cells with Janus and uniform films, the bare CNT cell exhibits a significant Li_2S peak after 10 cycles, indirectly indicating considerable LiPS leaching due to the limited LiPS adsorption capacity of CNT.[13]

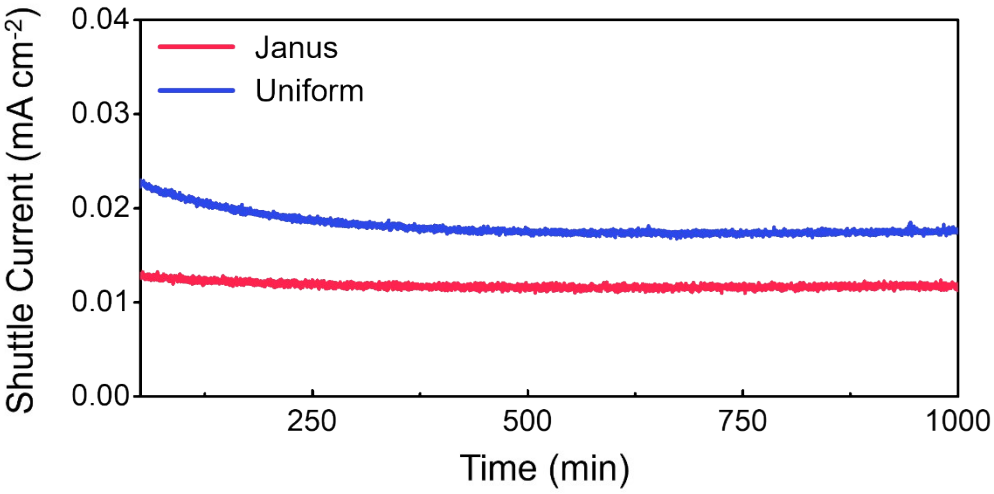

Fig. S19. Shuttle current in cells with Janus and uniform film cathode substrates. The shuttle current originates from oxidation/reduction reactions at the anode/cathode due to the diffusion of lithium polysulfides dissolved in the electrolyte. Shuttle current was measured by potentiostatic discharge at 2.38V. Both samples reached a steady state after 250 minutes, at which point the current was 0.012 mA cm^{-2} for the Janus and 0.017 mA cm^{-2} for the uniform film. The lower shuttle current in Janus is attributed to the delayed diffusion of lithium polysulfides within the Janus structure.[15]

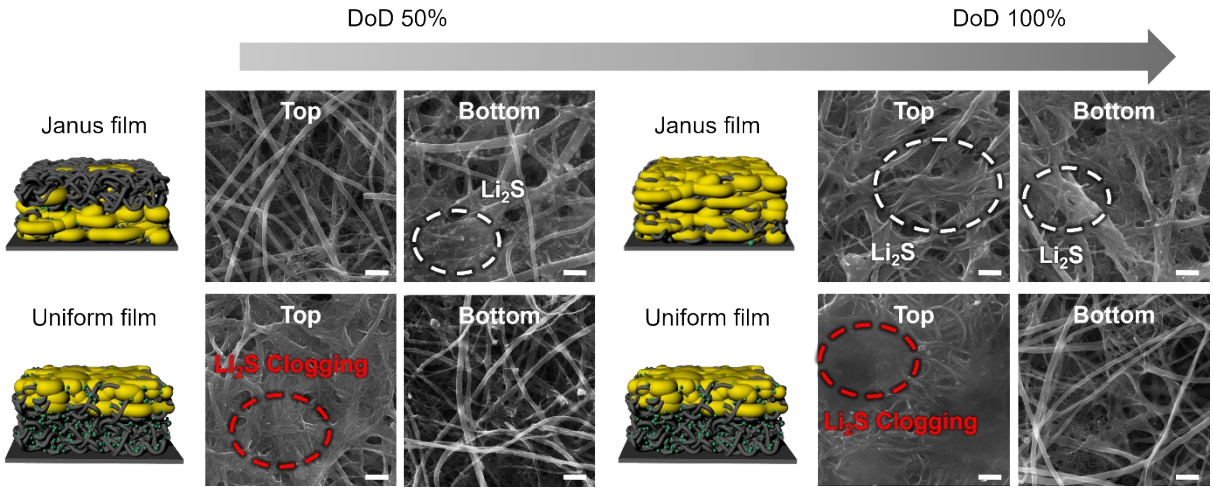

Fig. S20. Electron microscopy images of the surface and bottom layers of Janus and uniform film cathode substrates at various Depths of Discharge (DoD). The experiment was conducted by performing a potentiostatic discharge at 2.1V on each cathode substrate, which was loaded with 5 mg cm^{-2} of sulfur. During the precipitation of Li_2S from dissolved LiPS, the Janus film predominantly forms Li_2S in the lower layers initially, achieving a uniform distribution throughout the film at 100% DoD. Conversely, the uniform film predominantly exhibits Li_2S formation in the upper layers. This pattern of growth, due to the shorter diffusion path to the separator, might intensify the irreversible shuttling of LiPS during charge/discharge cycles. (Scale bar: 1 μm)

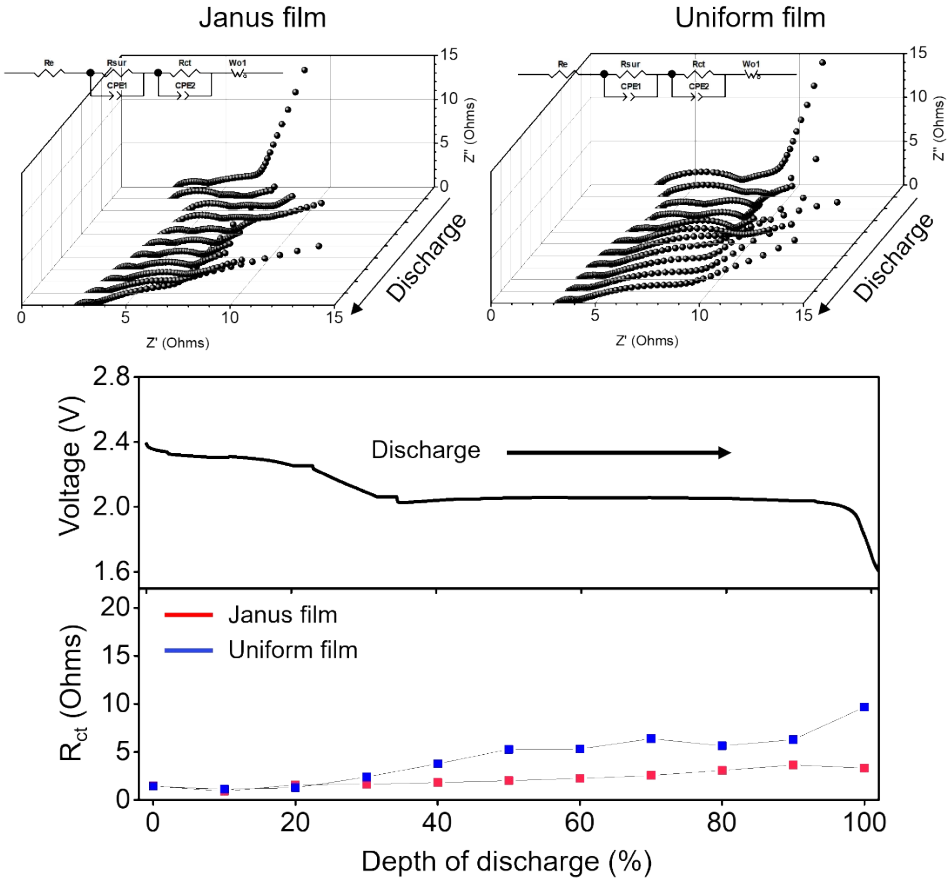

Fig. S21. Operando EIS analysis of Janus and uniform film cathode substrates at various Depths of Discharge (DoD): (Top panel) EIS spectra; (Bottom panel) Charge transfer resistance (R_{ct}).[16] Unlike the Janus film, the uniform film cathode exhibits a gradual increase in R_{ct} as DoD increases. This increase in resistance is attributed to the delayed diffusion caused by the top growth of Li_2S in the uniform film, similar to the observations in Fig. S19.

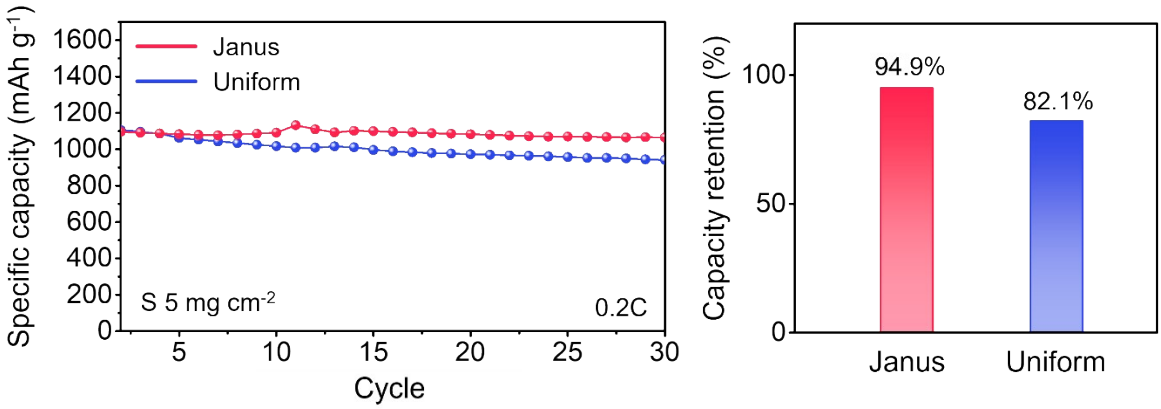

Fig. S22. Specific capacity over charge/discharge cycles for cells with Janus and uniform film cathode substrates, with a sulfur loading of 5 mg cm^{-2}. The initial discharge capacities are similar for both Janus and uniform films, at 1127 mAh g^{-1} and 1122 mAh g^{-1}, respectively. However, after 30 cycles, the capacity retention is 95% for the Janus film, compared to 82% for the uniform film. The lower capacity retention in the uniform film is attributed to relatively severe leaching of lithium polysulfides.

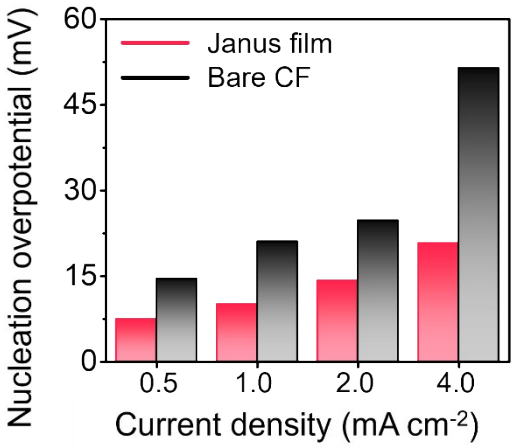

Fig. S23. Overpotentials for Li plating at various current densities. Overpotentials are lower in Janus films compared to bare carbon fiber.

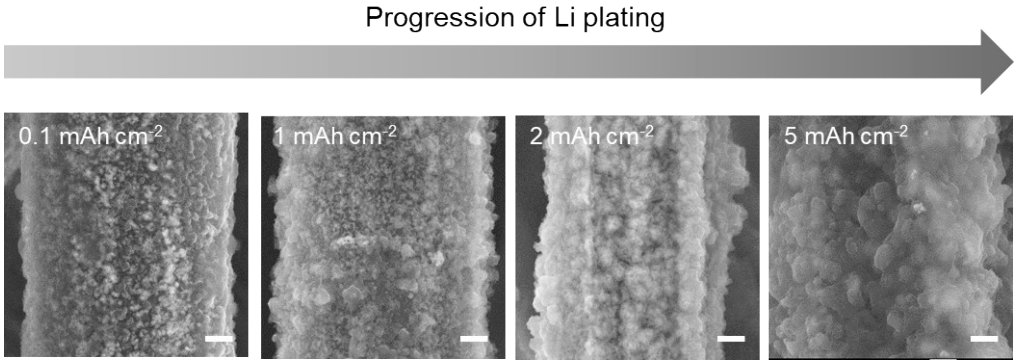

Fig. S24. Morphological changes on the Mo_2C-CF anode substrate surface with Li plating at increasing capacities. At 0.1 mAh cm^{-2}, an SEI layer forms; at 1 mAh cm^{-2}, Li nucleation occurs; at 2 mAh cm^{-2}, Li nuclei grow; and at 5 mAh cm^{-2}, a complete Li film forms. (Scale bar: 1 μm).[17]

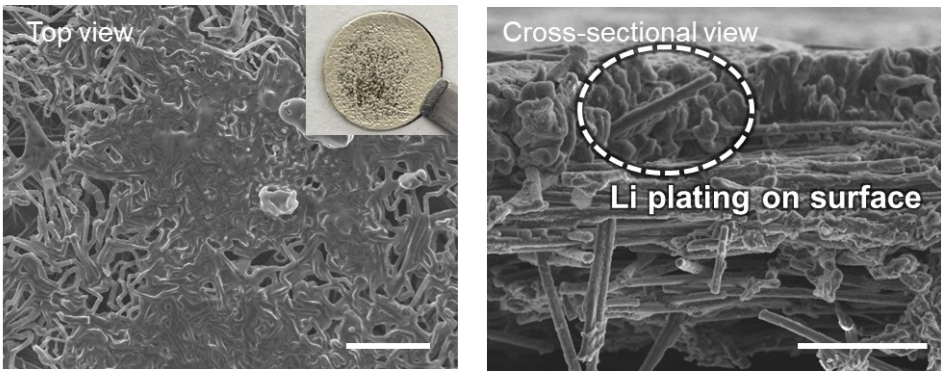

Fig. S25. Surface and cross-sectional SEM images of a bare CF anode substrate after lithium deposition at 10 mAh cm^{-2}. The cross-sectional SEM reveals that lithium does not fully plate throughout the carbon fibers, showing primarily top growth. This indicates that the diffusion of Li-ions is hindered by top growth, leading to incomplete Li deposition within the CF film. (Scale bar: left 10 μm, right 100 μm) The inset shows a digital camera image of the Li-deposited bare CF, highlighting the lithiophobic characteristics of the CF surface which result in uneven lithium deposition at high capacities.[18]

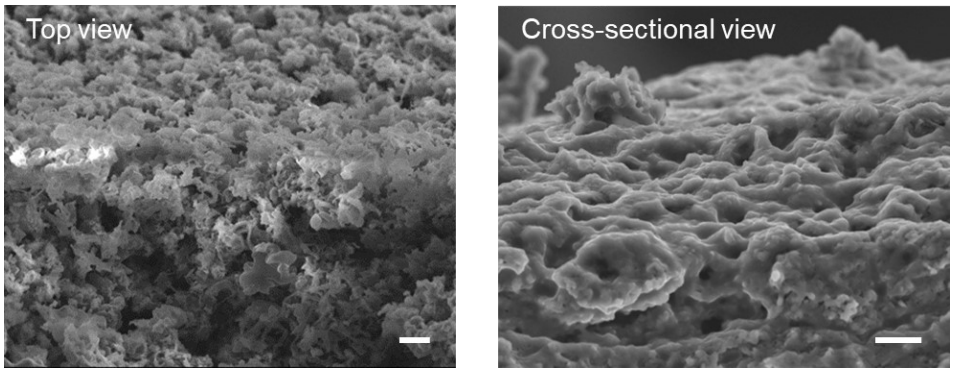

Fig. S26. Top-view and cross-sectional SEM images of a bare CF film anode substrate after Li plating. Moss-like Li dendrites are observed on the top of the electrode. (Scale bar: 10 μm)

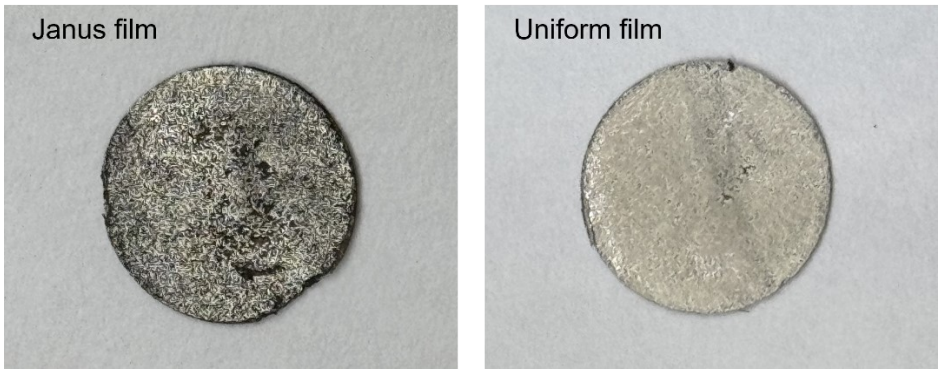

Fig. S27. Digital images of Janus and uniform film anode substrates after plating 10 mAh cm^{-2} of Li at 1 mA cm^{-2}. A lithium film is observed on the surface of the uniform film, indicating that top growth has taken place on this substrate.

Fig. S28. Thickness measurements of the Janus film anode substrate before and after Li plating, captured using a thickness measurement device. A difference of 0.004 μm is considered to be within the measurement error. Hence, the thickness of the film remains virtually unchanged after Li plating, confirming the complete accommodation of Li within the CF film

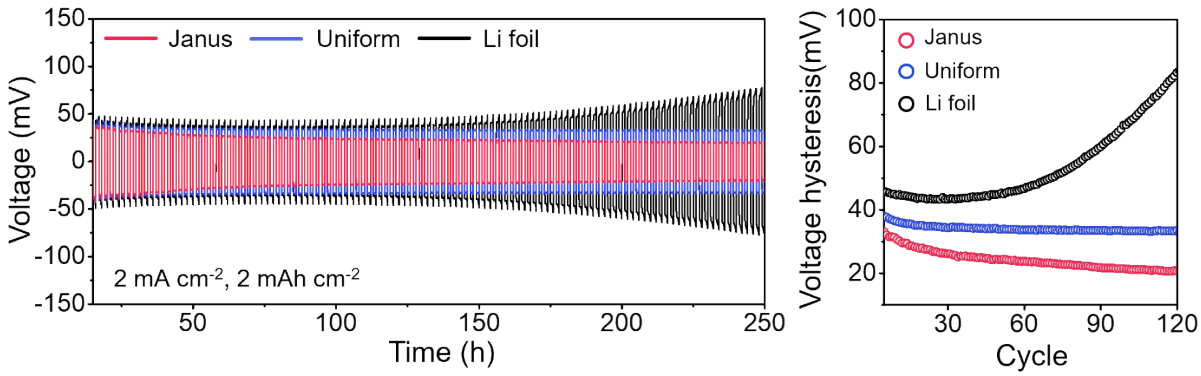

Fig. S29. (Left) Stripping/plating cycling stability of Janus film, uniform Mo_2C-CF film, and Li foil anodes at a current density of 2 mA cm^{-2} and a capacity of 2 mAh cm^{-2}. (Right) Voltage hysteresis of each anode over cycles. Both the Janus and uniform Mo_2C-CF film anodes demonstrate stable cycling for up to 250 hours (120 cycles). In contrast, the Li foil exhibits rapidly increasing instability with significant overpotential. The retention of low overpotential in the Janus films may result from effective Li nucleation at Mo_2C sites, which minimizes top growth during Li plating. Conversely, uniform Mo_2C-CF film anode shows relatively high overpotential due to incomplete utilization of Mo_2C for Li nucleation and the predominant top growth of Li.

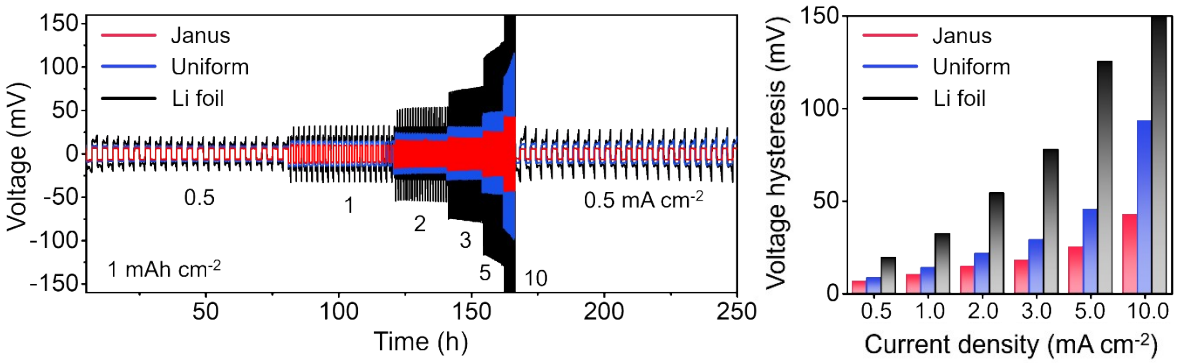

Fig. S30. (Left) Li plating/stripping cycling profiles at various current densities for Janus film, uniform Mo_2C-CF film, and Li foil anodes. (Right) Comparison of voltage hysteresis across these anodes. Janus film anodes show the lowest overpotentials and the smallest voltage hysteresis at all current densities.

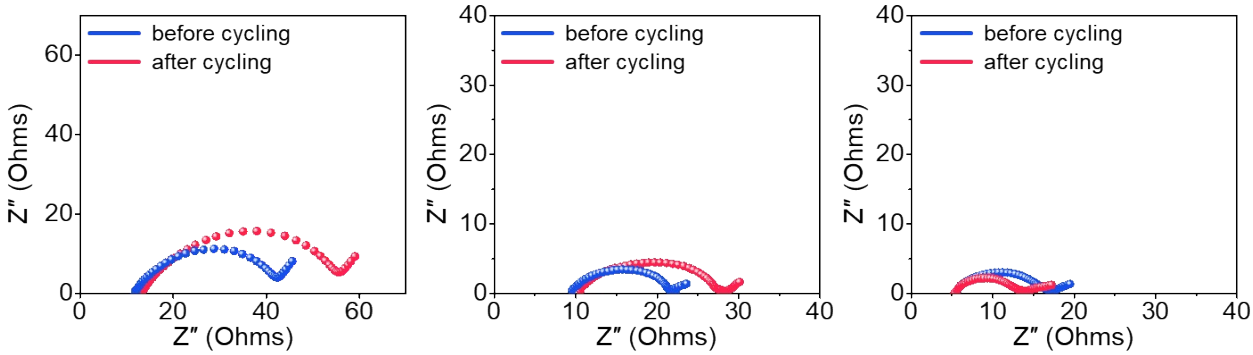

Fig. S31. (Left) EIS Spectra of Li foil, (Center) uniform Mo_2C-CF film, and (Right) Janus film before and after plating/stripping. The semicircle in the spectra indicates the charge transfer resistance (R_{ct}). Compared to Li foil, the uniform Mo_2C-CF film anode exhibits a lower R_{ct}, attributed to the higher surface area provided by the CF film host. However, after cycling, the uniform film shows an increase in R_{ct}, indicating top-growth. The Janus film anode displays the smallest R_{ct} and shows minimal increase after cycling, demonstrating enhanced Li plating/stripping accommodation within the film compared to the uniform film.

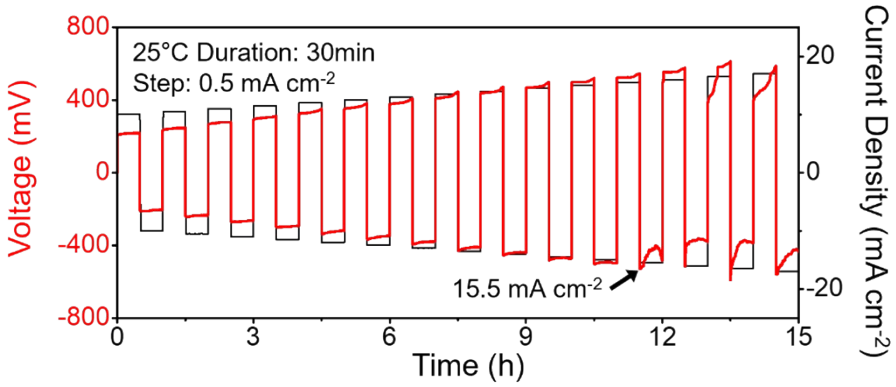

Fig. S32. Critical current density test of the Janus film anode. The Janus film symmetric cell is evaluated by stepwise increasing current densities with a step interval of 0.5 mA cm^{-2}.

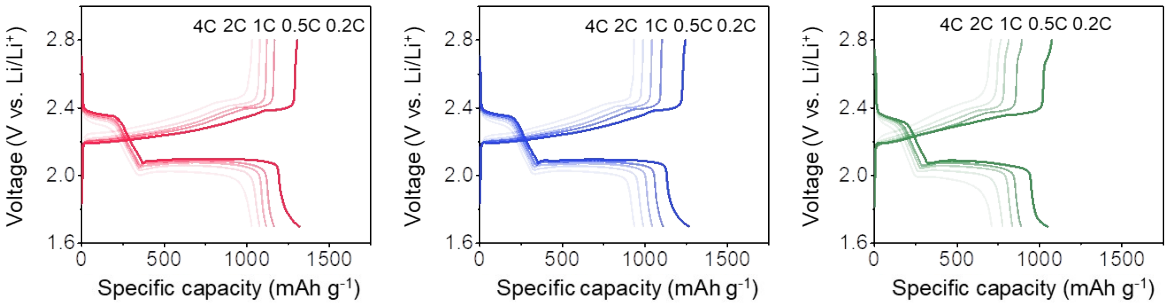

Fig. S33. Charge/discharge profiles at varying C-rates from 0.2 C to 4 C for (Left) S/Janus||Janus/Li full cell, (Center) S/Janus||Li cell, (Right) S/CNT||Janus/Li cell. S/Janus||Janus/Li full cell achieves a high discharge capacity of 1038 mAh g^{-1} even at 4 C.

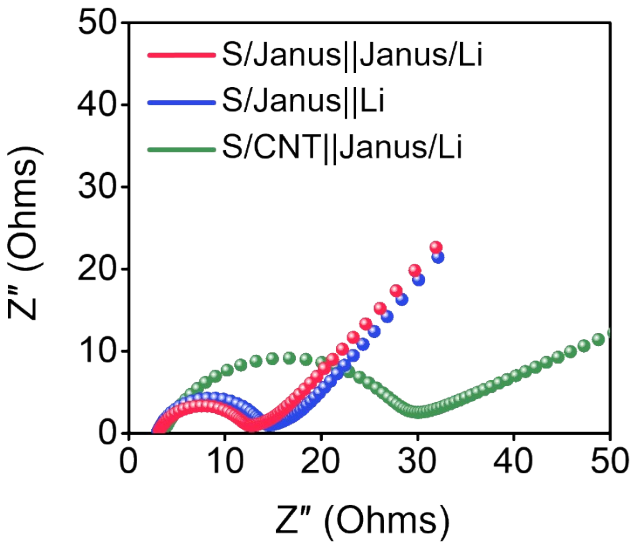

Fig. S34. EIS spectra of S/Janus||Janus/Li full cell, S/Janus||Li cell, and S/CNT|| Janus/Li cell. The S/Janus||Janus/Li full cell exhibits the smallest charge transfer resistance of 9.5 ohms, represented by the diameter of the semicircle, which corresponds to the high discharge capacity achieved at high rates.

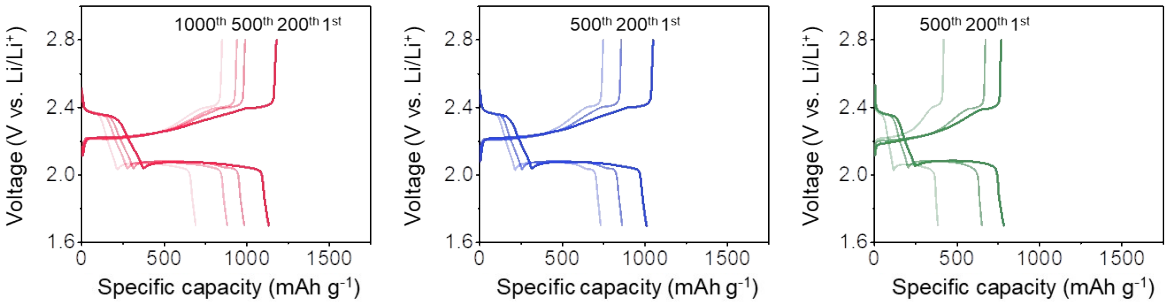

Fig. S35. Charge/discharge profiles at various cycles for (Left) S/Janus||Janus/Li full cell, (Center) S/Janus||Li cell, (Right) S/CNT||Janus/Li cell.

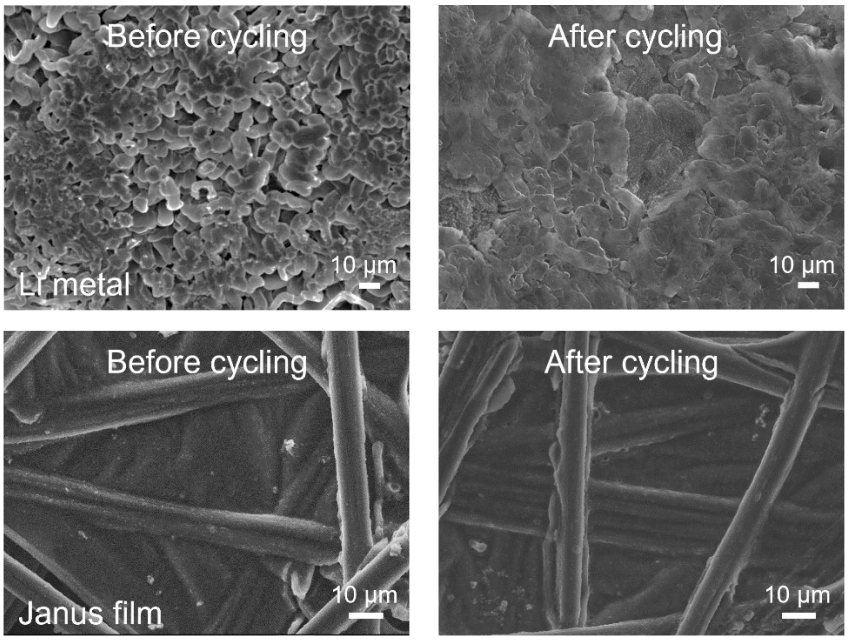

Fig. S36. (Top) *ex-situ* SEM images showing the Li plating morphology on Li metal anode and (Bottom) on Janus film anode, both before and after 200 cycles. A uneven and rough surface is observed on the Li metal compared to the Janus film.

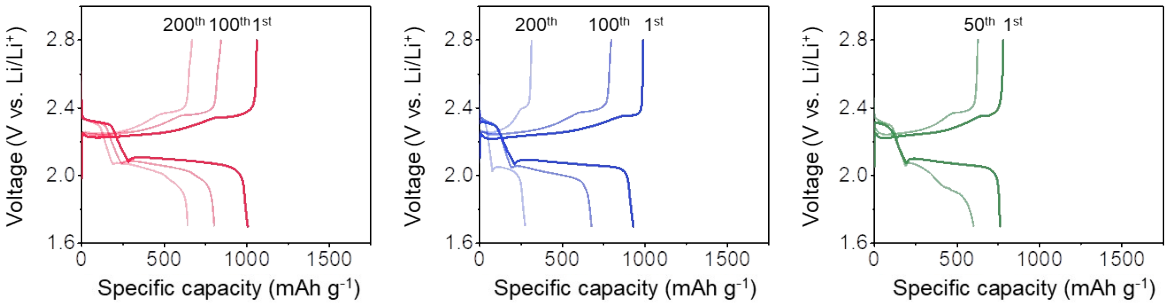

Fig. S37. Charge/discharge profiles at various cycles for for (Left) S/Janus||Janus/Li full cell, (Center) S/Janus||Li cell, (Right) S/CNT||Janus/Li cell, with a sulfur loading of 6 mg cm^{-2}. Despite the shuttle suppression effect in the S/Janus||Li cell from the Janus cathode, there is significant polarization and capacity loss due to the instability of Li metal during the stripping/plating processes. In the S/CNT||Janus/Li cell, severe LiPS leaching from the cathode and side reactions at the anode lead to significantly lower capacity and unstable plateaus.

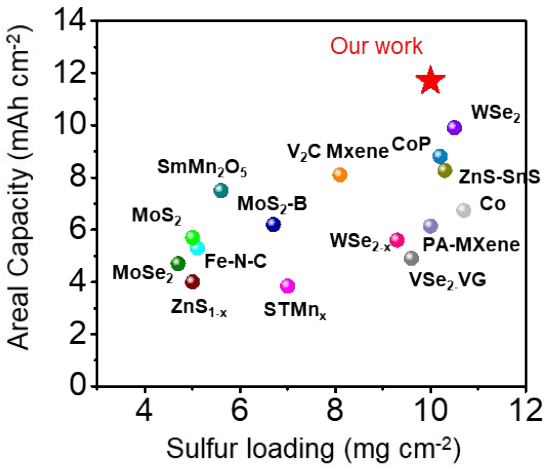

Fig. S38. Comparative analysis of areal capacity under high S loading conditions. Details are documented in Table S2. Previous research indicates a decrease in areal capacity with increased sulfur loading. Our work demonstrates superior areal capacities at ultra-high sulfur loadings, outperforming the capacities of the cells referenced.

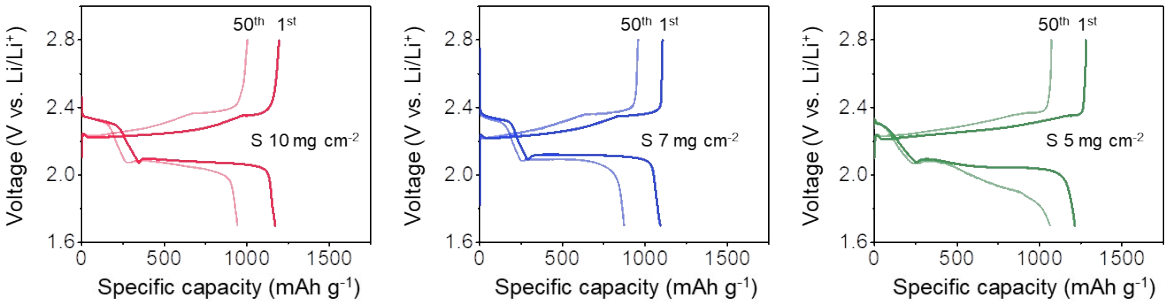

Fig. S39. Charge/discharge profiles at the initial and 50th cycle for the S/Janus||Janus/Li full cell at different sulfur loadings: (Left) 10 mg cm^{-2}, (Center) 7 mg cm^{-2}, and (Right) 5 mg cm^{-2}.

Table S1. Cell performance of various previous cathode host materials

Cathode material	Specific capacity (mAh g^{-1})	C-rate	Cycle	Decay per cylce (%)	ref
MgO/C	Approx. 1100	0.5	300	0.034	[13]
Ti_4O_7/S	850	2	500	0.06	[19]
$NiCo_2O_4$	872	1	400	0.065	[20]
Co-SnO_2@CNT	950	1	600	0.042	[21]
VC@NCNTs	1053	1	500	0.112	[22]
S/CNT-CoP-Vp	804	2	300	0.083	[23]
DHCP/S	840	1	500	0.077	[24]
QMo_2N-V	979	4	400	0.11	[25]
h-Co_4N@NC/S	917	2	400	0.051	[26]
c-a-MoO_3	1118	1	500	0.071	[27]
Nb_2O_5	1003	2	500	0.059	[28]

Table S2. Areal capacities achieved under high sulfur loading conditions in prior studies.

Cathode material	S loading (mg cm^{-2})	Areal capacity (mAh cm^{-2})	ref
Our work	10	11.7	
$SmMn_2O_5$	5.6	7.5	[29]
MoS_2	5.1	5.3	[30]
Fe-N-C	5	5.7	[31]
$MoSe_2$	4.7	4.7	[32]
ZnS_{1-x}	5	4	[33]
Perovskite $STMn_x$	7	3.84	[34]
MoS_2-B	6.7	6.2	[35]
WSe_2-x	9.3	5.6	[36]
VSe_2-VG	9.6	4.9	[37]
Co@NC	10.7	6.74	[38]
PA-MXene/CNT	10	6.14	[39]
WSe_2	10.5	9.9	[40]
V_2C-MXene	8.1	8.1	[41]

Table S3. Performance comparison between recent dual-functional host Li-S full cell studies.

Host	Areal capacity (mAh cm^{-2})	S loading (mg cm^{-2})	E/S ratio (μL mg^{-1})	N/P ratio	Cycle (retention %)	ref
Our work	6.3	6	4.4	2	50 (91.7)	
CoSe@C	5.3	6.2	4.5	4	100 (72.0)	[42]
1T′-$MoTe_2$	4.7	4.2	4.0	1.8	50 (61.8)	[43]
MCG-2	4.4	3.8	6.5	3	80 (85.5)	[44]
C25G75	3.3	6.0	6.0	2.4	200 (58.7)	[45]
WSe_2/NG	4.1	4.5	5	3	65 (82.2)	[40]
TiN-VN	5.5	5.6	15	2.9	100 (86.5)	[46]

Reference

1. C.-Y. Wang, T. Liu, X.-G. Yang, S. Ge, N. V. Stanley, E. S. Rountree, Y. Leng and B. D. McCarthy, *Nature*, 2022, **611**, 485-490.

2. J. Wu, Z. Ju, X. Zhang, A. C. Marschilok, K. J. Takeuchi, H. Wang, E. S. Takeuchi and G. Yu, *Adv. Mater.*, 2022, **34**, 2202780.

3. J. R. Owen, *Chem. Soc. Rev.*, 1997, **26**, 259-267.

4. R. Saroha, J. H. Oh, J. S. Lee, Y. C. Kang, S. M. Jeong, D.-W. Kang, C. Cho and J. S. Cho, *Chem. Eng. J.*, 2021, **426**, 130805.

5. P. Biswal, S. Stalin, A. Kludze, S. Choudhury and L. A. Archer, *Nano Lett.*, 2019, **19**, 8191-8200.

6. Y. Zhang, P. Zhao, Q. Nie, Y. Li, R. Guo, Y. Hong, J. Deng and J. Song, *Adv. Mater.*, 2023, **35**, 2211032.

7. J. Wan, J. Wu, X. Gao, T. Li, Z. Hu, H. Yu and L. Huang, *Adv. Funct. Mater.*, 2017, **27**, 1703933.

8. B. Yu, A. Huang, D. Chen, K. Srinivas, X. Zhang, X. Wang, B. Wang, F. Ma, C. Liu and W. Zhang, *Small*, 2021, **17**, 2100460.

9. Y. Wang, C. Li, X. Han, D. Liu, H. Zhao, Z. Li, P. Xu and Y. Du, *ACS Appl. Nano Mater.*, 2018, **1**, 5366-5376.

10. Y. Wen, Z. Shen, J. Hui, H. Zhang and Q. Zhu, *Adv. Energy Mater.*, 2023, **13**, 2204345.

11. C. Shen, K. Zhang, Y. You, H. Wang, R. Ning, Y. Qi, N. Li, C. Ding, K. Xie and B. Wei, *Nanoscale*, 2020, **12**, 13980-13986.

12. M. He, X. Li, W. Li, M. Zheng, J. Wang, S. Ma, Y. Ma, G. Yin, P. Zuo and X. Sun, *Chem. Eng. J.*, 2021, **411**, 128563.

13. X. Liang, C. Hart, Q. Pang, A. Garsuch, T. Weiss and L. F. Nazar, *Nat. Commun.*, 2015, **6**, 5682.

14. J. Qian, Y. Xing, Y. Yang, Y. Li, K. Yu, W. Li, T. Zhao, Y. Ye, L. Li and F. Wu, *Adv. Mater.*, 2021, **33**, 2100810.

15. D. Moy, A. Manivannan and S. R. Narayanan, *J. Electrochem. Soc.*, 2015, **162**, A1-A7.

16. Q. Fan, J. Jiang, S. Zhang, T. Zhou, W. K. Pang, Q. Gu, H. Liu, Z. Guo and J. Wang, *Adv. Energy Mater.*, 2021, **11**, 2100957.

17. F. Cheng, X. P. Yang, O. Ka, L. Wen, X. Q. Wang and W. Lu, *J. Mater. Chem. A*, 2023, **11**, 4205-4219.

18. W. Liu, D. C. Lin, A. Pei and Y. Cui, *J. Am. Chem. Soc.*, 2016, **138**, 15443-15450.

19. Q. Pang, D. Kundu, M. Cuisinier and L. F. Nazar, *Nat. Commun.*, 2014, **5**.

20. Y. T. Liu, D. D. Han, L. Wang, G. R. Li, S. Liu and X. P. Gao, *Adv. Energy Mater.*, 2019, **9**, 1803477.

21. Y. Yao, C. Chang, R. Li, D. Guo, Z. Liu, X. Pu and J. Zhai, *Chem. Eng. J.*, 2022, **431**, 134033.

22. J. Zheng, C. Guan, H. Li, Y. Xie, S. Li, J. Hu, K. Zhang, B. Hong, Y. Lai and J. Li, *Chem. Eng. J.*, 2022, **442**, 135940.

23. R. Sun, Y. Bai, Z. Bai, L. Peng, M. Luo, M. Qu, Y. Gao, Z. Wang, W. Sun and K. Sun, *Adv. Energy Mater.*, 2022, **12**, 2102739.

24. P. Zeng, X. Zhou, J. Peng, X. Huang, B. Chang, G. Chen, M. Chen, L. Zheng, Y. Pei and J. Su, *Adv. Funct. Mater.*, 2023, **33**, 2211818.

25. M. Yang, P. Liu, Z. Qu, F. Sun, Y. Tian, X. Ye, X. Wang, X. Liu and H. Li, *Nano Energy*, 2022, **104**, 107922.

26. Z. Sun, S. Vijay, H. H. Heenen, A. Y. S. Eng, W. Tu, Y. Zhao, S. W. Koh, P. Gao, Z. W. Seh and K. Chan, *Adv. Energy Mater.*, 2020, **10**, 1904010.

27. H. Lee, H. Nam and J. H. Moon, *Energy Storage Mater.*, 2024, 103551.

28. S. Yeom, H. Jo, H. Lee and J. H. Moon, *Energy Storage Mater.*, 2024, 103644.

29. L. Wang, W. Hua, X. Wan, Z. Feng, Z. Hu, H. Li, J. Niu, L. Wang, A. Wang and J. Liu, *Adv. Mater.*, 2022, **34**, 2110279.

30. Z. Cheng, Y. Chen, Y. Yang, L. Zhang, H. Pan, X. Fan, S. Xiang and Z. Zhang, *Adv. Energy Mater.*, 2021, **11**, 2003718.

31. J. Wang, W. Qiu, G. Li, J. Liu, D. Luo, Y. Zhang, Y. Zhao, G. Zhou, L. Shui and X. Wang, *Energy Storage Mater.*, 2022, **46**, 269-277.

32. C. Li, W. Ge, S. Qi, L. Zhu, R. Huang, M. Zhao, Y. Qian and L. Xu, *Adv. Energy Mater.*, 2022, **12**, 2103915.

33. J. Wang, Y. Zhao, G. Li, D. Luo, J. Liu, Y. Zhang, X. Wang, L. Shui and Z. Chen, *Nano Energy*, 2021, **84**, 105891.

34. W. Hou, P. Feng, X. Guo, Z. Wang, Z. Bai, Y. Bai, G. Wang and K. Sun, *Adv. Mater.*, 2022, 2202222.

35. D. Tian, X. Song, Y. Qiu, X. Sun, B. Jiang, C. Zhao, Y. Zhang, X. Xu, L. Fan and N. Zhang, *ACS nano*, 2021, **15**, 16515-16524.

36. H.-J. Li, K. Xi, W. Wang, S. Liu, G.-R. Li and X.-P. Gao, *Energy Storage Mater.*, 2022, **45**, 1229-1237.

37. H. Ci, J. Cai, H. Ma, Z. Shi, G. Cui, M. Wang, J. Jin, N. Wei, C. Lu and W. Zhao, *ACS nano*, 2020, **14**, 11929-11938.

38. Y. Li, W. Wang, B. Zhang, L. Fu, M. Wan, G. Li, Z. Cai, S. Tu, X. Duan and Z. W. Seh, *Nano Lett.*, 2021, **21**, 6656-6663.

39. B. Zhang, C. Luo, G. Zhou, Z. Z. Pan, J. Ma, H. Nishihara, Y. B. He, F. Kang, W. Lv and Q. H. Yang, *Adv. Funct. Mater.*, 2021, **31**, 2100793.

40. P. Wang, F. Sun, S. Xiong, Z. Zhang, B. Duan, C. Zhang, J. Feng and B. Xi, *Angew. Chem.*, 2022, **61**, e202116048.

41. L. Chen, Y. Sun, X. Wei, L. Song, G. Tao, X. Cao, D. Wang, G. Zhou and Y. Song, *Adv. Mater.*, 2023, **35**, 2300771.

42. J. He and A. Manthiram, *Adv. Energy Mater.*, 2020, **10**, 2002654.

43. J. He, A. Bhargav and A. Manthiram, *Adv. Energy Mater.*, 2022, **12**, 2103204.

44. P. Wang, B. Xi, Z. Zhang, N. Song, W. Chen, J. Feng and S. Xiong, *Small*, 2021, **17**, 2103744.

45. G. T. Yu and S. H. Chung, *Small*, 2023, **19**, 2303490.

46. Y. Yao, H. Wang, H. Yang, S. Zeng, R. Xu, F. Liu, P. Shi, Y. Feng, K. Wang and W. Yang, *Adv. Mater.*, 2020, **32**, 1905658.